Applied Catalysis B: Environmental 94 (2010) 272–280

Contents lists available at ScienceDirect

Applied Catalysis B: Environmental

journal homepage: www.elsevier.com/locate/apcatb

Study on highly visible light active Bi_2O_3 loaded ordered mesoporous titania

Sajjad Shamaila [a], Ahmed Khan Leghari Sajjad [a], Feng Chen [a], Jinlong Zhang [a,b,*]

[a] Key Laboratory for Advanced Materials and Institute of Fine Chemicals, East China University of Science and Technology, 130 Meilong Road, Shanghai 200237, PR China
[b] School of Chemistry and Materials Science, Guizhou Normal University, Guiyang 550001, PR China

ARTICLE INFO

Article history:
Received 24 September 2009
Received in revised form 23 November 2009
Accepted 1 December 2009
Available online 4 December 2009

Keywords:
Ordered mesoporous anatase
Bi_2O_3
Visible light
Photocatalysis
MO
2,4-DCP

ABSTRACT

The well-defined two-dimensional (2D) hexagonal mesoporous nanocrystalline anatase TiO_2 was synthesized by the nonhydrolytic evaporation-induced co-assembly (EISA) of non-ionic amphiphilic triblock-copolymer template, titanium tetrachloride and tetrabutyl titanate. The ordered mesoporous TiO_2 (M-TiO_2) was loaded with different % of Bi_2O_3 using the wet impregnation method. For comparison Degussa P25 impregnated with Bi_2O_3 was also prepared. The samples were characterized by thermogravimetric analysis (TGA), X-ray diffraction (XRD), Raman spectroscopy, transmission electron microscopy (TEM), UV–vis diffuse reflectance spectroscopy, photoluminescence spectra (PLS), Fourier transform infrared spectra (FT-IR), N_2 adsorption–desorption (BET) and X-ray photoelectron spectroscopy (XPS) techniques. XRD and Raman spectra showed the pore wall was composed of anatase. 1.0% Bi_2O_3 loaded M-TiO_2 revealed the well-ordered mesostructure. UV–vis diffuse reflectance spectroscopy measurements showed an extension of light absorption into the visible region. PLS analysis indicated that the electron–hole recombination rate have been effectively inhibited when Bi_2O_3 was loaded with ordered M-TiO_2. The photo oxidation efficiency was evaluated by methyl orange (MO) and 2,4-dichlorophenol (2,4-DCP) degradation under visible illumination. The samples loaded with different % of Bi_2O_3 showed higher photocatalytic activity than M-TiO_2 and Bi_2O_3 loaded P25. The catalyst exhibited high activity due to the Bi_2O_3-photosensitization and well-ordered 2D pore structure. The ordered mesoporous channels facilitate mass transport of the organic pollutants. TiO_2 could extend the spectral response from UV to visible region because of Bi_2O_3-photosensitization which make the Bi_2O_3 loaded M-TiO_2 photocatalyst visible light responsive.

1. Introduction

Efforts have been recently devoted to the development of functional nanoparticles, opening new opportunities for building up functional nanostructures. Titanium dioxide (TiO_2) has been of great interest for various applications in chemical sensor, catalyst and photocatalyst, and energy conversion fields [1–4]. The intrinsic properties of TiO_2 strongly depend on the morphology, type and size of its crystallites. Thus, the properties of high-surface area TiO_2 nanocrystals have attracted most scientific attention. TiO_2 nanocrystals are currently synthesized by the various methods such as hydrothermal [5], surfactant-directed [6,7] and sol–gel [8] approaches. Hydrothermal synthesis is directly carried out at elevated temperatures and typically results in nanocrystals agglomerates which are usually insoluble in common solvents. On the other hand, sol–gel preparations result in amorphous titanium dioxide, which is calcined at elevated temperatures in order to convert it into a crystalline form. To prevent agglomeration during thermal-induced crystallization, surfactants or amphiphilic block copolymers are commonly added into the sol–gel solution, which is very efficient in templating nanostructures. Block copolymers can self-assemble to form a variety of different nanostructures such as spheres, hexagonally packed cylinder and lamellae, with dimensions on the nanometer scale [9]. Especially, block copolymers are attractive as a template for the synthesis of nanostructural materials because of the ability to control both the size and the spatial organization by varying their composition and molecular weight [10,11]. An efficient method via evaporation-induced self-assembly (EISA) process is adopted to prepare ordered mesoporous titania [7,12,13]. Because the formation is kinetically controlled and greatly influenced by the atmospheric conditions of the laboratory, the reproducibility in obtaining high-quality mesoporous titania is still a challenge [14]. It is known that four variables should be carefully controlled during the EISA process [15] (a) the water amount, (b) the relative humidity, (c) the evaporation rate, and (d) the deposition and aging temperature.

Bi_2O_3 is an important photosensitizer with a direct band gap of 2.8 eV. As a result, the Bi_2O_3/TiO_2 could be easily activated by

* Corresponding author at: Key Laboratory for Advanced Materials and Institute of Fine Chemicals, East China University of Science and Technology, 130 Meilong Road, Shanghai 200237, PR China. Tel.: +86 21 64252062; fax: +86 21 64252062.
E-mail address: jlzhang@ecust.edu.cn (J. Zhang).

0926-3373/$ – see front matter © 2009 Elsevier B.V. All rights reserved.
doi:10.1016/j.apcatb.2009.12.001

visible lights owing to the photosensitization by Bi_2O_3 [16,17]. Design of TiO_2 with well-defined mesoporous structure is a promising way to achieve high photocatalytic activity since the ordered mesopore channels facilitate fast intraparticle molecular transfer [18,19]. While the large surface area may enhance the light harvesting, the adsorption for reactant molecules, and even the dispersion of Bi_2O_3 nanoparticles. Meanwhile, a high crystallization degree of photocatalysts is favorable for rapid transfer of photocharges from bulk to surface, which could inhibit the recombination between photoelectrons and holes, leading to enhanced quantum efficiency. Although mesoporous TiO_2 has already been synthesized by Antonelli and Ying [20] only a few papers concerning the ordered mesoporous TiO_2 with crystalline walls have been found in the literature [6,18,19]. To the best of our knowledge the ordered mesoporous TiO_2 was impregnated with Bi_2O_3 for the first time.

In this work, we report to prepare mesoporous nanocrystalline TiO_2 based on EISA method. M-TiO_2 was impregnated with Bi_2O_3 to make efficient use of visible light. The catalyst showed the superior activity as compared to M-TiO_2, Degussa P25 and impregnated Degussa P25 for the photodegradation of MO and 2,4-DCP. The factors affecting the photoactivity like photosensitization, the ordered mesoporous channels and the high crystallization degree are examined and discussed.

2. Experimental

2.1. Materials

Tetrabutyltitanate (TBT), titanium tetrachloride ($TiCl_4$), bismuth nitrate ($Bi(NO_3)_3{\cdot}5H_2O$), absolute ethanol and 2,4-DCP were AR grade. TBT and $TiCl_4$ were used as the titanium source while $Bi(NO_3)_3{\cdot}5H_2O$ was used as precursor of Bi_2O_3. All the chemicals were supplied from Shanghai Sinopharm Chemical Reagent Co. Ltd., China. Pluronic P123 [(Mw) 5800, $HO(CH_2CH_2O)_{20}(CH_2CHCH_3O)_{70}(CH_2CH_2O)_{20}H$, $EO_{20}PO_{70}EO_{20}$, abbreviated as P123] was received from Aldrich. Double distilled water was used throughout the experiments.

2.2. Catalyst preparation

The pure ordered mesoporous TiO_2 was synthesized by the EISA method using P123 surfactant as a template. In a typical synthesis 1.7 g of $TiCl_4$ and 3.0 g of $Ti(OBu)_4$ were added into 12.0 mL of ethanol solution containing 1.0 g of P123. A transparent sol was obtained after being stirred for 1.5 h at 0 °C, which was transferred into a Petri dish to form a uniform thin layer. After being aged at 40 and 100 °C for 24 h, respectively, the precursor was calcined at 350 °C for 4 h (0.5 °C/min) to remove template and other organic species. Samples containing 0.5, 1.0, 2.0, and 5.0 mol% Bi were prepared by the wet impregnation method. Mesoporous TiO_2 and $Bi(NO_3)_3{\cdot}5H_2O$ in different molar ratios were mixed in an ethanol solution and ground in an agate mortar. The mixture was dried at 60 °C for 1 h, followed by calcination at 350 °C for 4 h. The as-prepared samples were denoted as *x*% Bi_2O_3 loaded M-TiO_2, where *x*% refers to the Bi/Ti molar ratio. Degussa P25 was also impregnated by using above method and used for comparison.

2.3. Characterization

X-ray diffraction (XRD) patterns of all samples were collected in the range 20–80° (2θ) for wide angle XRD and 0.5–8° (2θ) for small angle XRD using a Rigaku D/MAX 2550 diffractometer (Cu Kα_1 radiation, λ = 1.5406 Å), operated at 40 kV and 100–200 mA. The crystallite size was estimated by applying the Scherrer equation to the full width at half-maximum (fwhm) of the (1 0 1) peak of anatase:

$$D = \frac{K\lambda}{\beta \cos\theta}$$

where β is the half-height width of the diffraction peak of anatase, K = 0.89 is a coefficient, θ is the diffraction angle, and λ is the X-ray wavelength corresponding to the Cu Kα irradiation. The UV–vis absorbance spectra were obtained for the dry-pressed disk samples using a Scan UV–vis spectrophotometer (Varian, Cary 500) equipped with an integrating sphere assembly, using $BaSO_4$ as the reflectance sample. The spectra were recorded at room temperature in air within the range 200–800 nm. The morphologies were observed by a transmission electron microscopy (TEM, JEOL JEM2010). Photoluminescence spectra (PLS) were recorded by Varian Cary Eclipse Fluorescence spectrophotometer under the excitation light at 270 nm. Raman spectra of the sample ware recorded by Renishaw in Via Raman spectrometer at room temperature with the excitation wavelength of 785 nm. FT-IR spectra were carried out by employing a Nicolet 740 FT-IR spectrometer equipped with a TGS detector and a KBr beam splitter. The instrument employed for XPS study was a Perkin-Elmer PHI 5000C ESCA System with Al Kα radiation operated at 250 W. TGA was performed on the Perkin-Elmer Pyris Diamond thermogravimetric analyzer.

2.4. Measurements of photocatalytic activities

The photocatalytic performance of catalyst was evaluated by using MO and 2,4-DCP. The photocatalytic degradation was carried out at 30–35 °C in a 100 mL quartz photochemical reactor. The initial concentration of MO and 2,4-DCP in a quartz reaction vessel was fixed at 25 mg L^{-1} with a catalyst loading of 1.0 g L^{-1}. A 1000 W halogen lamp was used as the light source. The short-wavelength components ($\lambda < 420$ nm) of the light were cut off using a cut-off glass filter. During the reaction, a water-cooling system cooled the water-jacketed photochemical reactor to maintain the solution at room temperature. The distance between the lamp and the center of quartz tube was 10 cm. Prior to illumination, the suspension was magnetically stirred in darkness for 30 min to establish adsorption–desorption equilibrium at room temperature. During irradiation, stirring was maintained to keep the mixture in suspension. At regular intervals, samples were withdrawn and centrifuged to separate photocatalyst for analysis. The extent of MO and 2,4-DCP decomposition was determined by measuring the absorbance value at approximately 465 nm and 283 nm respectively using a Cary100 UV/vis spectrophotometer.

3. Results and discussion

Highly ordered mesoporous titania was successfully synthesized by EISA method using TBT and $TiCl_4$ as titanium sources and triblock-copolymer P123 as template. For the efficient use of ordered M-TiO_2 in visible light source, it was impregnated with Bi_2O_3.

3.1. Thermogravimetric analysis

Thermogravimetric analysis (TGA) trace for the as synthesized MS-TiO_2 sample to replicate the calcination conditions, the analysis was carried out at a heating rate of 1 °C/min from 40 °C to 400 °C in air and held at a temperature of 400 °C for 4 h (Fig. 1). As shown in Fig. 1 below 150 °C, 10.4% mass loss is due to volatile species (water, ethanol) [21,22]. Between 150 °C and 270 °C a mass loss of 29.4% arises from the decomposition of the template. Some residual organic matter, such as amorphous carbon or carboxylate

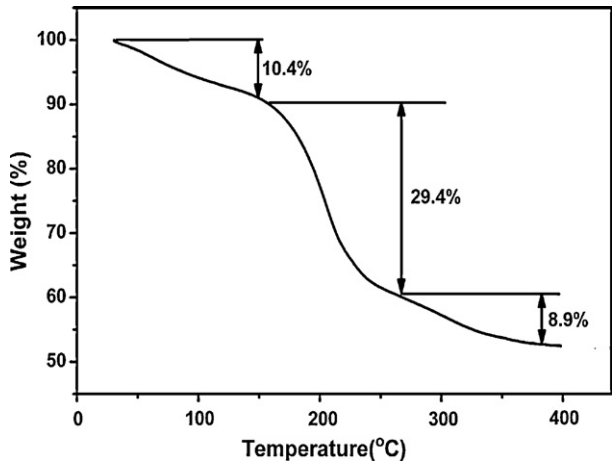

Fig. 1. TGA of as-prepared MS-TiO_2.

species and possibly hydroxyl groups, was removed at temperatures 270–370 °C with a mass loss of 8.9%. Above 370 °C mass loss is negligible. Based on this TGA trace and several related reports [14,21–23], the as synthesized sample was calcined at 350 °C for 4 h, the highest temperature calcination condition reported for thermally stable (2D) mesoporous titania prepared by using a triblock-copolymer as template.

3.2. X-ray diffraction

The small angle XRD patterns of M-TiO_2 product are presented in Fig. 2. SAXRD patterns show three well-resolved diffraction peaks with d-spacing ratios of $1 : \sqrt{3} : 2$ at 2θ angle of 0.5–2.0°, which can be indexed as the 100, 110, and 200 reflections of typical 2D hexagonal mesostructure [12,14,24,25], respectively. It clearly indicates a highly ordered mesostructured TiO_2. Three resolved diffraction peaks can also be observed after calcination at 350 °C for 4 h in air to remove the organic template, which indicate the highly ordered 2D hexagonal stable mesostructure. After calcination at 400 °C the XRD pattern becomes poor due to the collapse of mesostructure. The results showed that the M-TiO_2 mesostructure is thermally stable up to 350 °C. These results are well matched with the results quoted in [6,14,24] and further confirmed by the TEM observations. At 400 °C the small angle peak disappeared which is mainly related to the growth and coarsening of the anatase nanocrystallites [25].

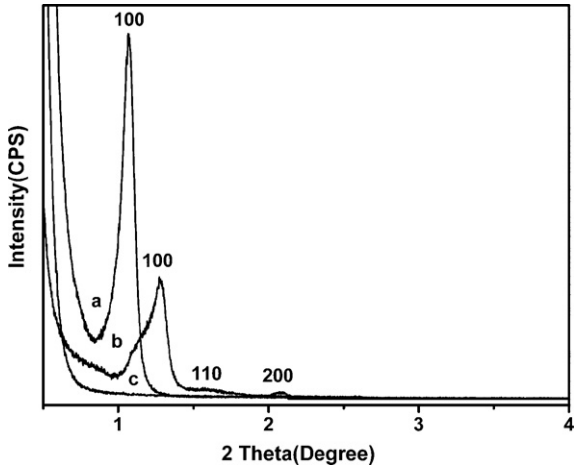

Fig. 2. Small angle XRD of M-TiO_2 (a) as-prepared; (b) calcined at 350 °C; (c) calcined at 400 °C.

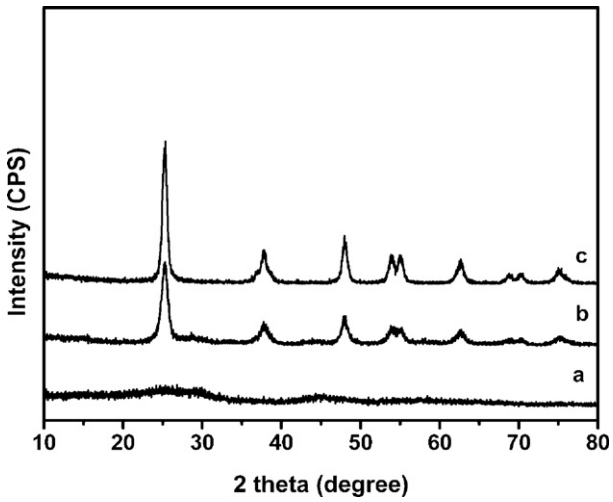

Fig. 3. Wide angle XRD of M-TiO_2 (a) as-prepared; (b) calcined at 350 °C; (c) calcined at 400 °C.

The wide angle XRD patterns in Fig. 3 of M-TiO_2 structure calcined at 350 °C in air showed broad diffraction peaks of anatase phase. These are characteristic diffractional peaks of anatase around 2θ of 25.2°, 37.9°, 47.8°, 53.8°, 55.0°, 62.7°, 68.8°, 70.3°, and 75.1° respectively [12,14,25]. It suggests the formation of TiO_2 nanocrystallites. As the calcination temperature increases, the diffraction peaks become stronger and narrow due to the growth in TiO_2 crystallinity. According to Scherrer's equation, the size of anatase nanocrystals increases from 6.2 nm to 7.7 nm on calcination from 350 °C to 400 °C. Fig. 4 showed the mesoporous TiO_2 loaded with different Bi contents calcined at 350 °C. All samples were calcined at 350 °C as the optimum calcination temperature. Because the Bi_2O_3 loaded M-TiO_2 calcined at that temperature displayed both the ordered mesoporous structure and highly crystallized anatase. WAXRD pattern shows intense reflections of anatase structure and some characteristic peaks of Bi_2O_3. Characteristic Bi_2O_3 diffractions with increasing intensity at 2θ values of 25.9°, 32.5° and 33.5° are observed with increasing Bi contents, indicating the increase in deposition. Mesoporous TiO_2 with a low Bi_2O_3 content (e.g. <2.0%) does not exhibit any Bi

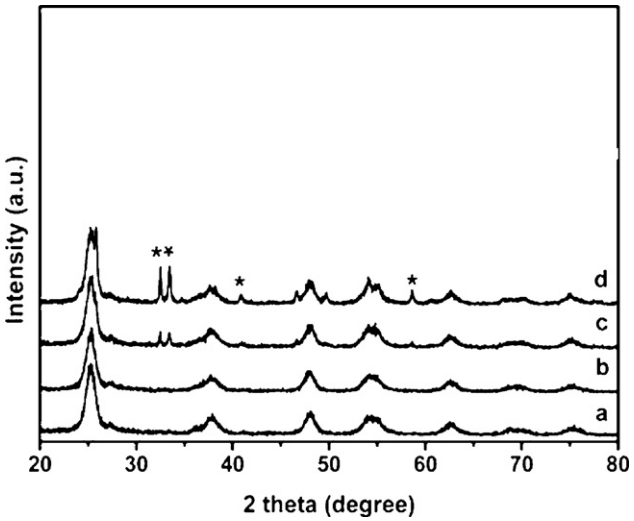

Fig. 4. Wide angle XRD of M-TiO_2 loaded with different % of Bi_2O_3 calcined at 350 °C (a) 0.5% Bi_2O_3 loaded M-TiO_2; (b) 1.0% Bi_2O_3 loaded M-TiO_2; (c) 2.0% Bi_2O_3 loaded M-TiO_2; (d) 5.0% Bi_2O_3 loaded M-TiO_2.

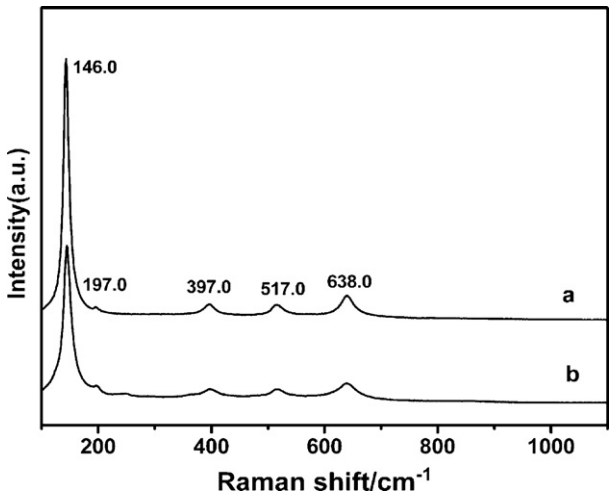

Fig. 5. Raman spectra of samples calcined at 350 °C (a) M-TiO_2; (b) 1.0% Bi_2O_3 loaded M-TiO_2.

characteristic diffraction which confirms the small nanoparticle size and high dispersion value. Characteristic Bi diffractions with increasing intensity and narrowing half-peak width are observed with increase in Bi content up to 5%, indicating the increasing particle size of 15 nm calculated by using Scherrer equation, results in blockage of mesopores and decrease of photocatalytic activity.

3.3. Raman spectra

Fig. 5 shows the Raman spectra of M-TiO_2 and 1.0% Bi_2O_3 loaded M-TiO_2. The Raman bands of TiO_2 as shown in Fig. 5 are appeared at 146.0 cm^{-1}, 197.0 cm^{-1}, 397.0 cm^{-1}, 517.0 cm^{-1} and 638.0 cm^{-1}. The typical bands of anatase are observed at 146.0 cm^{-1}, 196.0 cm^{-1}, 397.0 cm^{-1}, 516.0 cm^{-1} and 638.0 cm^{-1} assigned to the E_g, B_{1g}, A_{1g}, B_{2g}, and E_g vibrational modes of TiO_2, respectively [17,26,27]. The Raman bands become broader and weaker due to the presence of Bi_2O_3. This suggests that most of the incorporated Bi_2O_3 is highly dispersed over the TiO_2 mesoporous structure without forming large crystallized structures at 350 °C. These results are consistent with the XRD measurements.

3.4. Transmission electron microscopy

TEM images of ordered M-TiO_2 and 1.0% Bi_2O_3 loaded M-TiO_2 as shown in Fig. 6 viewed along the [001] direction confirmed that mesoporous TiO_2 products calcined at 350 °C exhibited a highly ordered 2D hexagonal regularity. Fig. 6b revealed the HRTEM images of 1.0% Bi_2O_3 loaded M-TiO_2. The anatase nanocrystals are clearly embedded in the matrix of the pore walls with random orientation. The average *d*-spacing of the lattice fringes measured from the TEM images is about 0.34 nm which agreed well with the $d_{1\,0\,1}$ value of 0.35 nm calculated from the corresponding wide angle XRD patterns. Such pore walls were comprised of highly crystallized anatase [28]. The size of anatase nanocrystal evaluated from the TEM images is about 6.5 nm, which is in consistent with the results calculated from wide angle XRD patterns. The average pore wall thickness evaluated is about 3.6 nm. The TEM image in Fig. 6c of the 1.0% Bi_2O_3 loaded M-TiO_2 calcined at 350 °C displayed highly ordered mesoporous channels with average diameter of 7.8 nm. No significant Bi_2O_3 particles were observed in the pore channels and on the outer surface, implying the extremely high dispersion of the Bi_2O_3 particles [29], which was consistent with the above conclusion from XRD patterns.

3.5. UV–vis absorption spectra

The UV–vis absorption spectra of M-TiO_2, Degussa P25, 1.0% Bi_2O_3 loaded M-TiO_2 and 1.0% Bi_2O_3 loaded P25 were measured to determine their optical absorption characteristic. A clear comparison of the loaded and neat samples (M-TiO_2, Degussa P25) is shown in Fig. 7. UV–vis absorption spectra revealed that the M-TiO_2 and P25 displayed no significant absorbance for visible lights due to the large energy gap of TiO_2 (3.2 eV). It is evident that 1.0% Bi_2O_3 loaded M-TiO_2 sample extends the absorption edge to longer wavelengths [30]. It is well known that intrinsic transitions give sharp increases in absorbance whereas impurity or defect state transitions give absorption tails in semiconductors [31].

3.6. Photoluminescence spectra

PL emission spectra have been widely used to investigate the change of surface states of TiO_2, the efficiency of charge carrier trapping, immigration and transfer to understand the fate of electron–hole pairs in semiconductor particles [32]. Fig. 8 showed the comparison of the room temperature photoluminescence spectra with 270 nm excitation wavelength in the range of 350–550 nm for M-TiO_2 and Bi_2O_3 loaded M-TiO_2 [33,34]. As for the pure M-TiO_2 the well-resolved peaks at 421 nm, 443 nm, 456 nm, 468 nm, 486 nm, and 512 nm were observed. All these peaks are ascribed to surface traps [35,36]. The excitonic PL intensity of these samples decreases as: M-TiO_2 > 0.5% Bi_2O_3 loaded M-TiO_2 > 2.0% Bi_2O_3 loaded M-TiO_2 > 1.0% Bi_2O_3 loaded M-TiO_2. It can be clearly observed from Fig. 8 that Bi_2O_3 loaded TiO_2 showed decrease in the intensity of PL spectra as compared to M-TiO_2 which indicated the

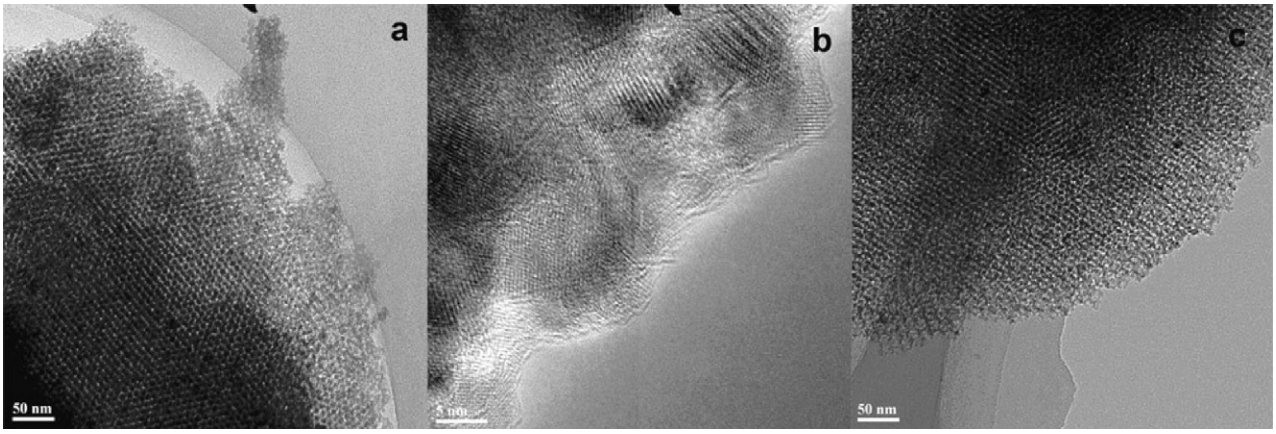

Fig. 6. TEM and HRTEM of samples calcined at 350 °C (a) TEM image of M-TiO_2; (b) HRTEM image of 1.0% Bi_2O_3 loaded M-TiO_2; (c) TEM image of 1.0% Bi_2O_3 loaded M-TiO_2.

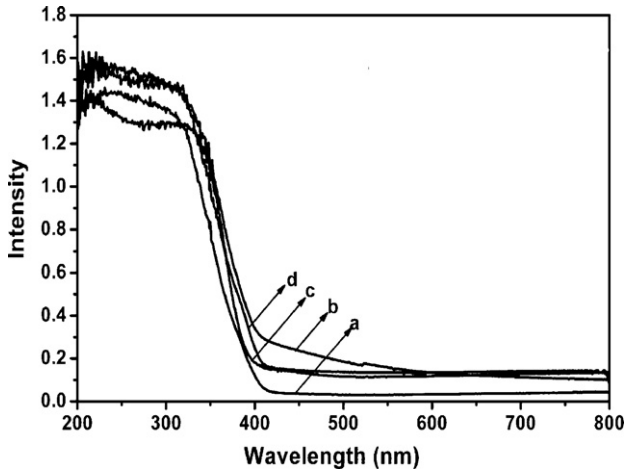

Fig. 7. UV–vis diffuse reflectance spectra of samples calcined at 350 °C (a) Degussa P25; (b) 1.0% Bi_2O_3 loaded M-TiO_2; (c) M-TiO_2; (d) 1.0% Bi_2O_3 loaded Degussa P25.

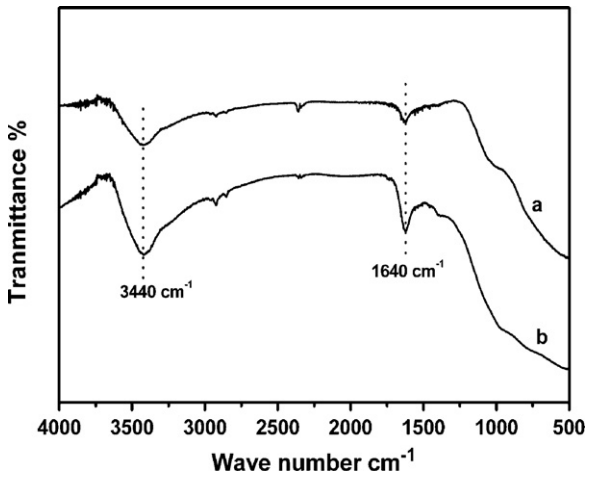

Fig. 9. FT-IR spectra of samples calcined at 350 °C (a) M-TiO_2; (b) 1.0% Bi_2O_3; loaded M-TiO_2.

decrease in trap states on surface of M-TiO_2. M-TiO_2 incorporated with an appropriate amount of Bi_2O_3 may slow the radiative recombination process of photogenerated electrons and holes in TiO_2. The slower recombination process of photogenerated charges will benefit the photocatalytic reaction [37].

3.7. Fourier transform infrared spectra

The surface hydroxyl groups on titania have been recognized to play an important role on the photocatalytic reaction since they can inhibit the recombination of photogeneration charges and interact with photogenerated holes to produce active oxygen species. The FT-IR spectra of the M-TiO_2 and 1.0% Bi_2O_3 loaded M-TiO_2 are shown in Fig. 9. The broad and strong peak at 1640 cm^{-1} is ascribed to the bending vibration absorption of free water, and the peaks at 3200–3600 cm^{-1} are attributed to the stretching vibration absorption of hydroxyl function groups (TiO_2–OH bonds) which is often believed that such groups arise from the hydrolysis process [38]. FT-IR investigation confirms that pure titania has the less surface OH group density. The surface OH group density increases with Bi_2O_3 loading. The larger surface hydroxyl group density will lead to enhancement of the photocatalytic activity. Because they can interact with photogenerated holes, which gives better charge transfer and inhibits the recombination of electron–hole pairs [37].

3.8. N_2 adsorption–desorption

N_2 adsorption–desorption isotherms of 2D hexagonal M-TiO_2 calcined at 350 °C as shown in Fig. 10 have typical type IV curves with a sharp capillary condensation step at relative high pressure which suggest a very narrow pore size distribution. The hysteresis loop H_1 type showed uniform cylindrical pore geometry [14,39]. The pore size calculated from the adsorption data using the BJH model is 7.8 nm as shown in inset of Fig. 10 consistent with that evaluated from TEM images. The calculated BET specific surface area is 186 m^2/g. The large surface area may enhance the light harvesting, the adsorption for reactant molecules, and even the dispersion of Bi_2O_3 nanoparticles.

3.9. X-ray photoelectron spectroscopy

Quantitative XPS analysis is performed on 1.0% Bi_2O_3 loaded M-TiO_2 powder after thermal treatment at 350 °C for 4 h. Fig. 11 shows the typical full survey and high-resolution spectra for the Ti 2p, O 1s and Bi 4f region. 1.0% Bi_2O_3 loaded M-TiO_2 contains only Ti, O, Bi and C elements. The C element can be ascribed to the adventitious hydrocarbon from the XPS instrument itself.

High-resolution XPS spectrum of Bi 4f region is shown in Fig. 11b. The peaks centered at 164.2 eV and 158.9 eV were

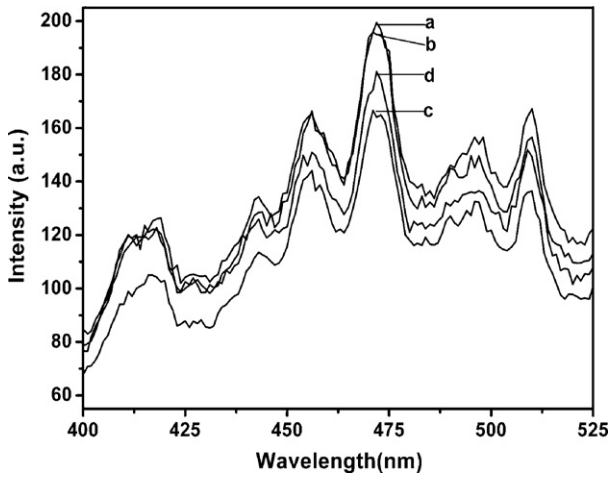

Fig. 8. Photoluminescence spectra of samples calcined at 350 °C (a) M-TiO_2; (b) 0.5% Bi_2O_3 loaded M-TiO_2; (c) 1.0% Bi_2O_3 loaded M-TiO_2; (d) 2.0% Bi_2O_3 loaded M-TiO_2.

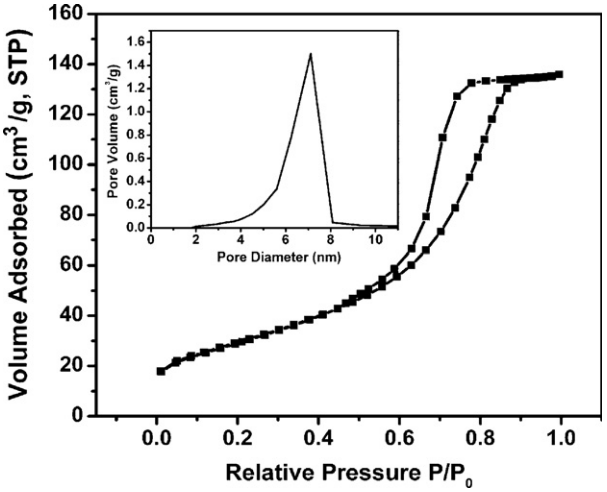

Fig. 10. N_2 adsorption–desorption isotherm of M-TiO_2 calcined at 350 °C (inset figure is pore size distribution of M-TiO_2 calcined at 350 °C).

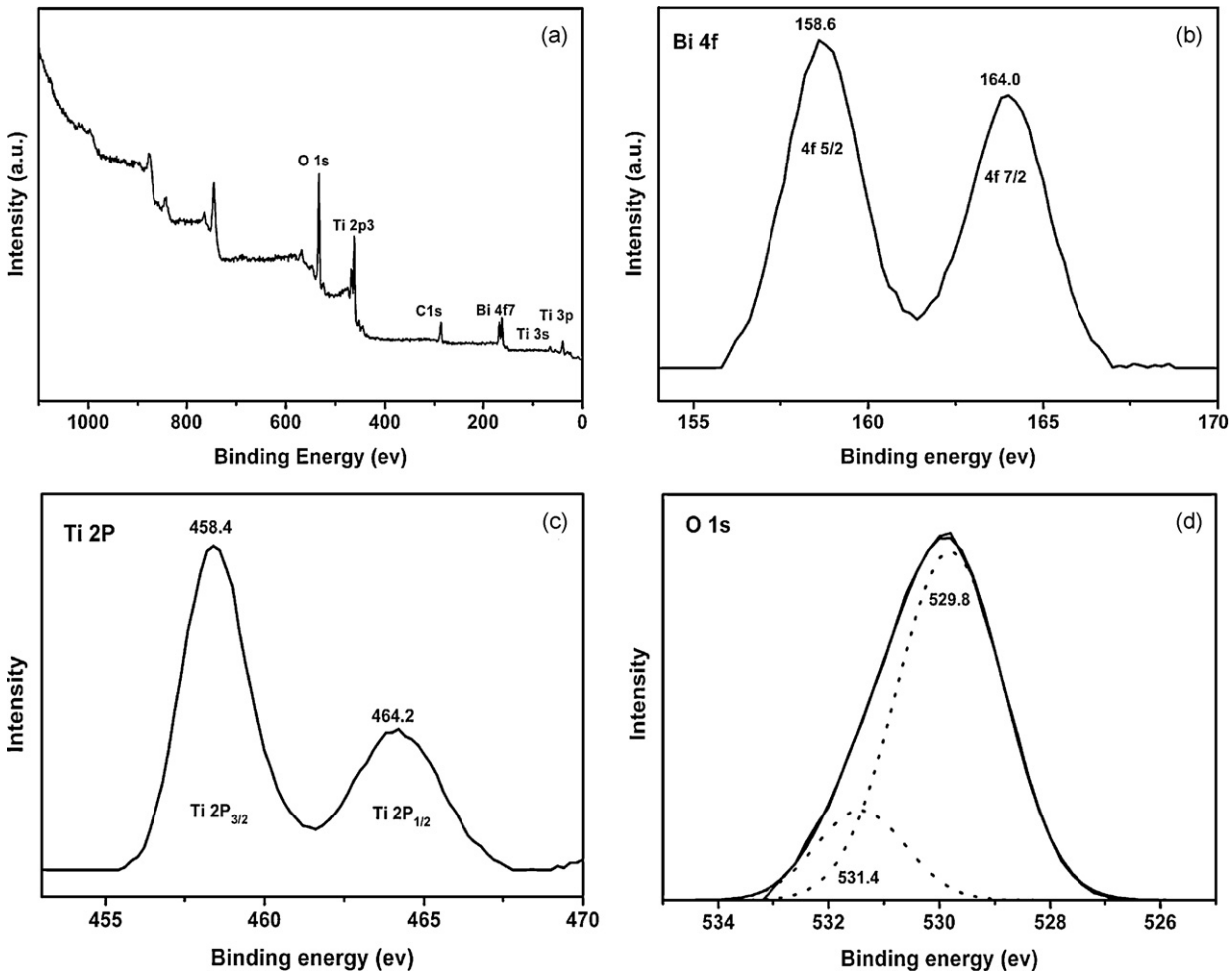

Fig. 11. XPS studies of 1.0% Bi_2O_3 loaded M-TiO_2 (a) full XPS spectra; (b) high-resolution XPS spectra of Bi 4f region; (c) Ti 2p; (d) O 1s.

assigned to Bi $4f_{5/2}$ and Bi $4f_{7/2}$ region [40]. These binding energy values were same as those obtained from pure Bi_2O_3. Therefore, XPS spectra demonstrated that all the Bi species in samples were present in the form of Bi_2O_3.

In Ti 2p orbital two peaks were assigned to $2p_{1/2}$ and $2p_{3/2}$ as shown in Fig. 11c. The Ti $2p_{1/2}$ and Ti $2p_{3/2}$ spin–orbital splitting photoelectrons for the sample were located at the binding energies of about 464.2 eV and 458.4 eV respectively, which was in agreement with the reported literature values [41,42]. Therefore, this result means that the Ti oxidation state remain unchanged showing the presence of Ti^{4+}. There was no Ti^{3+} species observed in XPS. O 1s region was also split into some contributions as shown in Fig. 11d. Two spectra were observed: the first peak of 529.8 eV assigned to Ti–O in TiO_2, whereas the second shoulder one at 531.4 eV is ascribed to the oxygen attached to bismuth (Bi–O bond) [43]. The high binding energy of Bi–O bond is due to the fact that the oxygen atom in a stronger Ti–O covalent bond carries a higher effective negative charge than that in a weaker Bi–O bond [44,45]. Some researchers suggested that this shoulder peak is associated with hydroxyl groups [46]. The presence of Bi_2O_3 exerted no significant influence on the XPS spectra in either the Ti 2p level or the O 1s level. It confirmed that the composite consisted of titania with Bi_2O_3 loading [47].

3.10. Mechanism of the formation of mesoporous TiO_2 with well-ordered pore morphology and Bi_2O_3 assisted photocatalytic process

Scheme 1 illustrates the possible mechanism of the synthetic procedure and Bi_2O_3 assisted photocatalytic process. It is suggested that $TiCl_4$ can react with EtOH to form $Ti(Cl)_{4-x}(OEt)_x$ ($x \approx 2$) species [48], resulting in a highly acid mother solution (pH ≈ 1). Upon the addition of $Ti(OBu)_4$, serving as both a major titanium source and an extra oxygen donor, the acidity of the solution is reduced. Meanwhile oligomers formulated as $TiX_x(O\text{-}H)_yO_{2-(x+y)/2}$ (X = OR or Cl; $x \approx 0.3$–0.7; $y \approx 0$–0.2) are obtained [49]. Ti–O–Ti bridges may partially result from the condensation between Ti–Cl and Ti–OR. With the evaporation of ethanol and following thermopolymerization and calcinations to remove the template, TiO_2 with a regular pore distribution is formed. When the mesoporous TiO_2 is formed it is loaded with different % of Bi_2O_3. Due to Bi_2O_3 loading it becomes visible light responsive. Scheme 1 also shows the proposed degradation pathway of Bi_2O_3 assisted photocatalytic process. As the band gap of Bi_2O_3 is 2.85 eV, it can be excited by light with wavelength less than 435 nm [50,51]. However, the photocatalytic activity of pure Bi_2O_3 is very low because of the high electron–hole recombination rate in Bi_2O_3 [52]. The valence band of Bi_2O_3 is lower than that of titania [53], the Bi_2O_3–TiO_2 heterojunctions formed in the composite will promote the photo generated holes in bismuth oxide to be transferred to the upper lying valence bands of titania as shown in Scheme 1. In addition, molecular oxygen O_2 can be served as the scavenger of the electrons to yield the superoxide radical anion O_2^- and hydrogen peroxide H_2O_2. This process is thermodynamically feasible [54]. Recombination rate of photo-induced electron–hole pairs was reduced and much more holes were captured to induce photocatalytic reactions. Any factor that suppresses the electron–hole recombination will therefore enhance the photocatalytic activity. As the recombination rate of photo-induced electron–hole

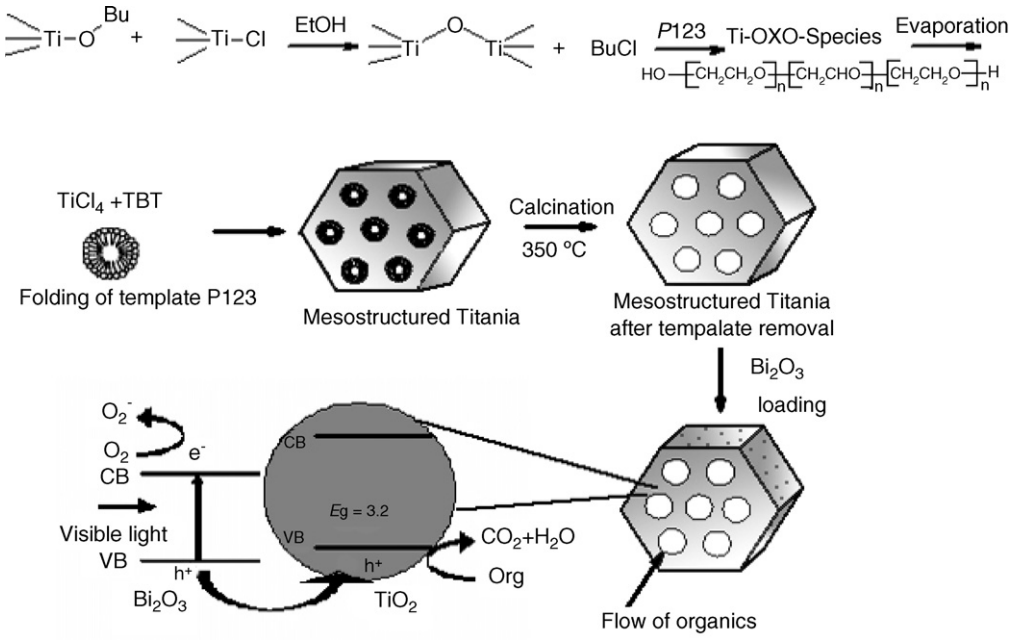

Scheme 1. Possible mechanism of the formation of mesoporous TiO_2 with well-ordered pore morphology and Bi_2O_3 assisted photocatalytic process.

pairs was reduced and much more holes were captured to induce photocatalytic reactions. Thus, the photocatalytic activity of Bi_2O_3–TiO_2 composite enhanced a lot as compared to the M-TiO_2, P25, 1.0% Bi_2O_3 loaded P25.

3.11. Photocatalytic activity

The photoactivities for MO and 2,4-DCP in dark in the presence of the photocatalyst and under visible light irradiation in the absence of the photocatalyst were evaluated. It was found that there was no degradation for the MO and 2,4-DCP in the dark and in the presence of the photocatalyst. There was no degradation observed for MO and 2,4-DCP when the solution was placed under visible light radiation without the addition of photocatalyst powder. As shown in Fig. 12, 1.0% Bi_2O_3 loaded M-TiO_2 degraded 80.0% MO and 1.0% Bi_2O_3 loaded Degussa P25 degraded only about 32% while pure mesoporous TiO_2 and Degussa P25 showed 14.0% and 6.0% degradation in visible light respectively. 1.0% Bi_2O_3 loaded TiO_2 degraded 62.0% 2,4-DCP and 1.0% Bi_2O_3 loaded Degussa P25 degraded about 25.0% while pure TiO_2 and Degussa P25 showed 10.0% and 5.0% degradation in visible light respectively as shown in Fig. 13. Modification of TiO_2 with 1.0% Bi_2O_3 loading resulted in superior photocatalytic activity as compared to pure Degussa P25 and 1.0% Bi_2O_3 loaded Degussa P25. So the Bi_2O_3-photosensitization play an important role in degradation process. The ordered mesoporous channels facilitated the diffusion of reactant molecules and also provided the larger surface area for Bi_2O_3 distribution. 1.0% Bi_2O_3 loaded M-TiO_2 showed the red-shift in the absorption wavelength range and reduced the electron–hole recombination. Consequently, there is an optimum concentration of loaded ions to make the thickness of space charge layer substantially equal to the light penetration depth. As the concentration of dopant ions increases towards the optimum amount, the surface barrier becomes higher, and the space charge region becomes narrower. The electron–hole pairs within the region are efficiently separated by the large electric field before recombination.

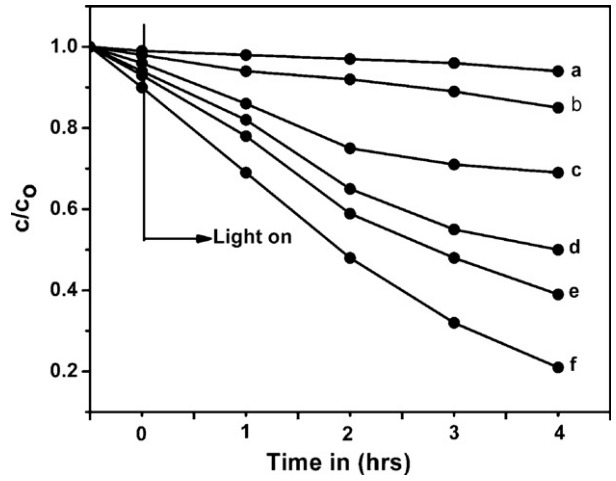

Fig. 12. Degradation profile of MO by using (a) Degussa P25; (b) M-TiO_2; (c) 1.0% Bi_2O_3 loaded Degussa P25; (d) 0.5% Bi_2O_3 loaded M-TiO_2; (e) 2.0% Bi_2O_3 loaded M-TiO_2; (f) 1.0% Bi_2O_3 loaded M-TiO_2 calcined at 350 °C.

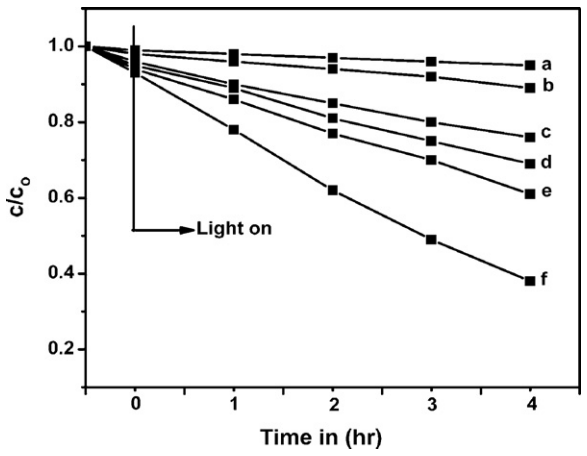

Fig. 13. Degradation profile of 2,4-DCP by using (a) Degussa P25; (b) M-TiO_2; (c) 1.0% Bi_2O_3 loaded Degussa P25; (d) 0.5% Bi_2O_3 loaded M-TiO_2; (e) 2.0% Bi_2O_3 loaded M-TiO_2; (f) 1.0% Bi_2O_3 loaded M-TiO_2 calcined at 350 °C.

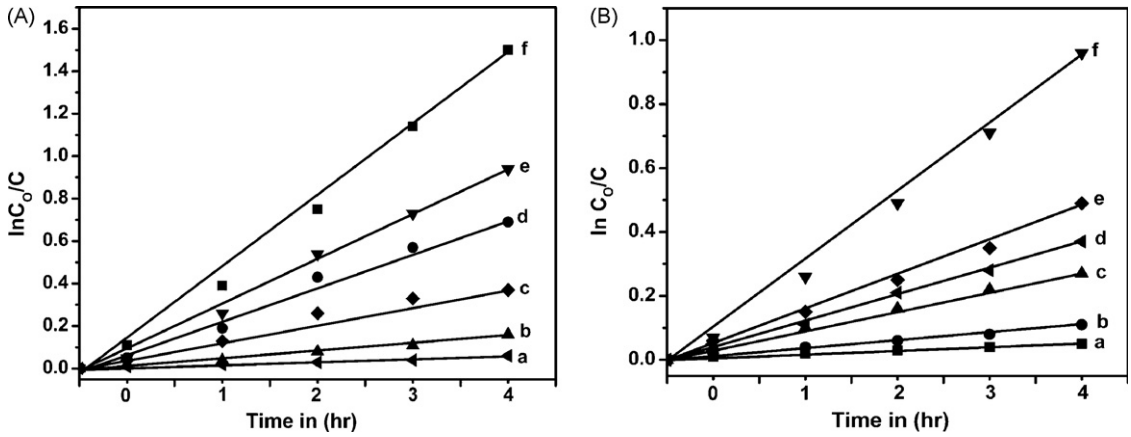

Fig. 14. Kinetic study during degradation of MO (A) 2,4-DCP (B) by using (a) Degussa P25; (b) M-TiO_2; (c) 1.0% Bi_2O_3 loaded Degussa P25; (d) 0.5% Bi_2O_3 loaded M-TiO_2; (e) 2.0% Bi_2O_3 loaded M-TiO_2; (f) 1.0% Bi_2O_3 loaded M-TiO_2 calcined at 350 °C.

Table 1
Apparent rate constant data for different samples.

Samples	P25	Pure mesoporous TiO_2	1.0%Bi_2O_3 loaded P25	0.5%Bi_2O_3 loaded TiO_2	2% Bi_2O_3 loaded TiO_2	1% Bi_2O_3 loaded TiO_2
MO	0.0002	0.0006	0.0015	0.0028	0.0038	0.0068
2,4-DCP	0.0002	0.0004	0.0012	0.0015	0.0021	0.0040

High Bi content (Bi/Ti molar ratio > 1.0%) was harmful for the activity because of the agglomeration of the Bi_2O_3 particles. The high Bi contents rather than facilitate charge transport and reduce charge recombination, the large nanoparticles may act as the centers of electron–hole recombination and reduce quantum efficiency [47,55]. The lower dispersion of Bi_2O_3 reduced its photosentisizing effect, leading to the poor harvesting for visible lights. The big Bi_2O_3 particles resulted in partial blockage of mesoporous channels which may retard the diffusion of reactant molecules because the ordered mesoporous channels facilitated the diffusion of reactant molecules. Due to the high concentration of loaded ions, the space charge region becomes very narrow and the penetration depth of light into TiO_2 greatly exceeds the space charge layer. Therefore, the recombination of the photogenerated electron–hole pairs in semiconductor becomes easier. The crystallization of anatase facilitated the rapid transfer of photoelectrons from bulk to the surface, which could effectively inhibit the recombination between photoelectrons and holes, leading to enhanced quantum efficiency [56,57].

Generally, the photocatalytic activity of a photocatalyst for the photooxidation of organic compounds is mainly related to two factors: (1) the position of valence band of the photocatalyst and (2) the mobility of photogenerated carriers [58,59]. In the hybridized valence band of Bi_2O_3 loaded TiO_2, the photogenerated holes possessed a high mobility, which contributed to the high activity of the photocatalyst. Considering the structure of Bi_2O_3 loaded TiO_2, the Bi–O in Bi_2O_3 loaded TiO_2 may serve as the active electron donor sites, which enhances the electron transfer to O_2 and eliminates the recombination of the photogenerated electron–hole pairs [60].

3.12. Kinetics of reaction

The photodegradation reaction kinetic of organic pollutents can be described by a modified Langmuir–Hinshelwood model according to the reports [56,61]. The apparent rate constant (k_{app}) has been chosen as the basic kinetic parameter for the different photocatalysts, since it enables one to determine a photocatalytic activity independent of the previous adsorption period in the dark and the concentration of solute remaining in the solution. The apparent first order kinetic equation (1) is used to fit experimental data shown in Fig. 14:

$$\ln\left(\frac{C_0}{C}\right) = k_{app}t \quad (1)$$

where C is the concentration of solute remaining in the solution at irradiation time of t, and C_0 is the initial concentration at $t = 0$ [62]. The variations in $\ln(C_0/C)$ as a function of irradiation time are given in Fig. 13. The calculated apparent rate constant (k_{app}) data for Bi_2O_3 loaded TiO_2 samples, pure mesoporous titania, P25 and Bi_2O_3 loaded P25 are exhibited in Table 1. It confirmed that k_{app} enhanced by incorporating TiO_2 with Bi_2O_3.

4. Conclusions

In this work ordered mesoporous TiO_2 based on the EISA method with 2D hexagonal structure was successfully prepared and a new approach was adopted to make it visible light active by loading the pure ordered mesoporous TiO_2 with different % of Bi_2O_3. 1.0% Bi_2O_3 loaded M-TiO_2 sample showed superior photocatalytic activity and degraded 80.0% MO and 62.0% 2,4-DCP as compared to 1.0% Bi_2O_3 loaded Degussa P25. 1.0% Bi_2O_3 loaded M-TiO_2 showed maximum response to visible light due to the reduced electron–hole recombination and extended spectral response to the visible region. Photosensitizing effect of Bi_2O_3 with the porous structure plays an important role to make this an efficient catalyst. The presence of highly crystalline anatase facilitated the transfer of photoelectrons from bulk to surface and thus could inhibit the recombination between photoelectrons and holes, leading to the enhanced quantum efficiency. Pure mesoporous TiO_2 has the large surface area for Bi_2O_3 dispersion and light harvesting. This work provides a new pathway to design and fabricate novel photoactive materials for practical application in environmental cleaning.

Acknowledgments

This work has been supported by Science and Technology Commission of Shanghai Municipality (07JC14015); National Nature Science Foundation of China (20773039, 20977030); National Basic Research Program of China (973 Program, 2007CB613301, 2010CB732306), and the Ministry of Science and Technology of China (2006AA06Z379, 2006DFA52710). Shamaila Sajjad and Sajjad Ahmed Khan Leghari thank Higher Education Commission (Pakistan) for support.

References

[1] R. Al-Rasheed, D.J. Cardin, Appl. Catal. A: Gen. 246 (2003) 39–48.
[2] L. Miao, S. Tanemura, S. Toh, K. Kaneko, M. Tanemura, Appl. Surf. Sci. 238 (2004) 175–179.
[3] Q. Sheng, S. Yuan, J. Zhang, F. Chen, Micropor. Mesopor. Mater. 87 (2006) 177–184.
[4] A.L. Linsebigler, G.Q. Lu, J.T. Yates, Chem. Rev. 95 (1995) 735–758.
[5] Y. Kotani, T. Matoda, A. Matsuda, T. Kogure, M. Tatsumisago, T. Minami, Mater. Chem. 11 (2001) 2045–2048.
[6] S. Yuan, Q. Sheng, J. Zhang, F. Chen, M. Anpo, Q. Zhang, Micropor. Mesopor. Mater. 79 (2005) 93–99.
[7] P.D. Yang, D.Y. Zhao, D.I. Margolese, B.F. Chmelka, G.D. Stucky, Chem. Mater. 11 (1999) 2813–2826.
[8] J. Gutierrez, A. Tercjak, I. Garcia, L. Peponi, I. Mondragon, Nanotechnology 19 (2008) 155601–155607.
[9] S. Forster, M. Antonietti, Adv. Mater. 10 (1998) 195–217.
[10] S. Yuan, Q. Sheng, J. Zhang, F. Chen, M. Anpo, Mater. Lett. 58 (2004) 2757–2760.
[11] H.C. Kim, X. Jia, C.M. Stafford, D.H. Kim, T.J. McCarthy, M. Tuominen, C.J. Hawker, T.P. Russell, Adv. Mater. 13 (2001), 795-797.
[12] P.D. Yang, D.Y. Zhao, D.I. Margolese, B.F. Chmelka, G.D. Stucky, Nature 396 (1998) 152–155.
[13] S. Yuan, Q. Sheng, J. Zhang, F. Chen, M. Anpo, W. Dai, Catal. Lett. 107 (2006) 19–24.
[14] S.Y. Choi, M. Mamak, N. Coombs, N. Chopra, G.A. Ozin, Adv. Funct. Mater. 14 (2004) 335–344.
[15] E.L. Crepaldi, G.J. de A.A. Soler-Illia, D. Grosso, F. Cagnol, F. Ribot, C. Sanchez, J. Am. Chem. Soc. 125 (2003) 9770–9786.
[16] Y. Bessekhouad, D. Robert, J.V. Weber, Catal. Today 101 (2005) 315–321.
[17] M. Kanga, Y. Ko, M. Jeon, S. Lee, S. Choung, J. Park, S. Kim, S. Choi, J. Photochem. Photobiol. A 173 (2005) 128–136.
[18] H.X. Li, Z.F. Bian, J. Zhu, Y.N. Huo, H. Li, Y.F. Lu, J. Am. Chem. Soc. 129 (2007) 4538–4539.
[19] J.C. Yu, X.C. Wang, X.Z. Fu, Chem. Mater. 16 (2004) 1523–1530.
[20] D.M. Antonelli, J.Y. Ying, Angew. Chem. Int. Ed. 34 (1995) 2014–2017.
[21] D. Grosso, G.J.A.A. Soler-Illia, F. Babonneau, C. Sanchez, P.A. Albouy, A. Brunet-Bruneau, A.R. Balkenende, Adv. Mater. 13 (2001) 1085–1090.
[22] P.C.A. Alberius, K.L. Frindell, R.C. Hayward, E.J. Kramer, G.D. Stucky, B.F. Chmelka, Chem. Mater. 14 (2002) 3284–3294.
[23] H. Li, Z. Bian, J. Zhu, Y. Huo, H. Li, Y. Lu, J. Am. Chem. Soc. 129 (2007) 4538–4539.
[24] B.Z. Tian, X.Y. Liu, B. Tu, C.Z. Yu, J. Fan, L.M. Wang, S.H. Xie, G.D. Stucky, D.Y. Zhao, Nat. Mater. 2 (2003) 159–163.
[25] D.L. Li, H.S. Zhou, I. Honma, Nat. Mater. 3 (2004) 65–72.
[26] I.R. Beattie, T.R. Gilson, J. Chem. Soc. A (1969) 2322–2327.
[27] A.K.L. Sajjad, S. Shamaila, B. Tian, F. Chen, J. Zhang, Appl. Catal. B: Environ. 91 (2009) 397–405.
[28] J.C. Yu, X.C. Wang, L. Wu, W.K. Ho, L.Z. Zhang, G.T. Zhou, Adv. Funct. Mater. 14 (2004) 1178–1183.
[29] Z. Bian, J. Zhu, S. Wang, Y. Cao, X. Qian, H. Li, J. Phys. Chem. C 112 (2008) 6258–6262.
[30] Y. Wu, G. Lu, S. Li, J. Phys. Chem. C 113 (2009) 9950–9955.
[31] N. Serpone, E. Pelizzetti, Photocatalysis: Fundamentals and Application, Edition, Wiley/Interscience, New York, 1989, p. 123.
[32] H. Yamashita, Y. Ichihashi, S.G. Zhang, Y. Matsumura, Y. Souma, T. Tatsumi, M. Anpo, Appl. Surf. Sci. 121 (1997) 305–309.
[33] Y. Cong, J. Zhang, F. Chen, M. Anpo, D. He, J. Phys. Chem. C 111 (2007) 10618–10623.
[34] Y. Wu, H. Liu, J. Zhang, F. Chen, J. Phys. Chem. C 113 (2009) 14689–14695.
[35] T. Toyoda, T. Hayakawa, K. Abe, T. Shigenari, Q. Shen, J. Lumin. 87–89 (2000) 1237–1239.
[36] B.S. Liu, X.J. Zhao, L.P. Wen, Mater. Sci. Eng. B 134 (2006) 27–31.
[37] J. Xu, Y. Ao, D. Fu, C. Yuan, Appl. Surf. Sci. 255 (2008) 2365–2369.
[38] T. Lopez, J.A. Moreno, R. Gomez, X. Bokhimi, J.A. Wang, H.Y. Madeira, G. Pecchi, P. Reyes, J. Mater. Chem. 12 (2002) 714–718.
[39] W. Dong, Y. Sun, C.W. Lee, W. Hua, X. Lu, Y. Shi, S. Zhang, J. Chen, D. Zhao, J. Am. Chem. Soc. 129 (2007) 13894–13904.
[40] Y. Schuhl, H. Baussart, R. Delobel, M. Le Bras, J. Leroy, L.G. Gengembre, J. Rimblot, J. Chem. Soc., Faraday Trans. 79 (1983) 2055–2069.
[41] M. Srivasan, T. White, Environ. Sci. Technol. 41 (2007) 4405–4409.
[42] H.M. Liu, W.S. Yang, Y. Ma, Y.A. Cao, J.N. Yao, J. Zhang, T.D. Hu, Langmuir 19 (2003) 3001–3005.
[43] Y. Wang, Y. Wang, Y. Meng, H. Ding, Y. Shan, X. Zhao, X. Tang, J. Phys. Chem. C 112 (2008) 6620–6626.
[44] M.W. Chu, M. Ganne, M.T. Caldes, L. Brohan, J. Appl. Phys. 91 (2002) 3178–3187.
[45] C. Jovalekic, M. Pavlovic, P. Osmokrovic, L. Atanasoska, Appl. Phys. Lett. 72 (1998) 1051–1053.
[46] J.C. Dupin, D. Gonbeau, P. Vinatier, A. Levasseur, Phys. Chem. Chem. Phys. 2 (2000) 1319–1324.
[47] J.H. Xin, S.M. Zhang, G.D. Qi, X.C. Zheng, W.P. Huang, S.H. Wu, React. Kinet. Catal. Lett. 86 (2005) 291–298.
[48] A. Vioux, Chem. Mater. 9 (1997) 2292–2299.
[49] J. Blanchard, F. Ribot, C. Sanchez, P.V. Bellot, A. Trokiner, J. Non-Cryst. Solids 265 (2000) 83–97.
[50] W.D. He, W. Qin, X.H. Wu, H.L. Ning, Mater. Lett. 61 (2007) 4100–4102.
[51] W.D. He, W. Qin, X.H. Wu, X.B. Ding, L. Chen, Z.H. Jiang, Thin Solid Films 515 (2007) 5362–5365.
[52] M.A. Fox, M.T. Dulay, Chem. Rev. 93 (1993) 341–357.
[53] T.P. Gujar, V.R. Shinde, C.D. Lokhande, Mater. Res. Bull. 41 (2006) 1558–1564.
[54] Y.H. Ao, J.J. Xu, D.G. Fu, X.W. Shen, C.W. Yuan, Sep. Purif. Technol. 61 (2008) 436–441.
[55] A. Hagfeldt, M. Gratzel, Chem. Rev. 95 (1995) 49–68.
[56] M.R. Hoffmann, S.T. Martin, W.Y. Choi, D.W. Bahnemannt, Chem. Rev. 95 (1995) 69–96.
[57] A. Fujishima, T.N. Rao, D.A. Tryk, J. Photochem. Photobiol. C 1 (2000) 1–21.
[58] K. Ikarashi, J. Sato, H. Kobayashi, N. Saito, H. Nishiyama, Y. Inoue, J. Phys. Chem. B 106 (2002) 9048–9053.
[59] J. Sato, H. Kobayashi, Y. Inoue, J. Phys. Chem. B 107 (2003) 7970–7975.
[60] W.F. Yao, H. Wang, X.H. Xu, X.F. Cheng, J. Huang, S.X. Shang, X.N. Yang, M. Wang, Appl. Catal. A 243 (2003) 185–190.
[61] C. Lettmann, K. Hindenbrand, H. Kisch, W. Macyk, W.F. Maier, Appl. Catal. B: Environ. 32 (2001) 215–227.
[62] J. Matos, J. Laine, J.M. Herrmann, Appl. Catal. B: Environ. 18 (1998) 281–291.